Food Chemistry 327 (2020) 127000

Contents lists available at ScienceDirect

Food Chemistry

journal homepage: www.elsevier.com/locate/foodchem

The presence of iron oxide nanoparticles in the food pigment E172

Linn Voss[a], I-Lun Hsiao[b,c], Maximilian Ebisch[d], Janja Vidmar[e], Nadine Dreiack[a], Linda Böhmert[a], Valerie Stock[a], Albert Braeuning[a], Katrin Loeschner[e], Peter Laux[a], Andreas F. Thünemann[d], Alfonso Lampen[a], Holger Sieg[a,*]

[a] German Federal Institute for Risk Assessment, Max-Dohrn-Str. 8-10, 10589 Berlin, Germany
[b] School of Food Safety, College of Nutrition, Taipei Medical University, Taipei, Taiwan
[c] Master Program in Food Safety, College of Nutrition, Taipei Medical University, Taipei, Taiwan
[d] German Federal Institute of Material Research and Testing (BAM), Unter den Eichen 87, 12205 Berlin, Germany
[e] National Food Institute, Technical University of Denmark, Kemitorvet, Building 201, 2800 Kgs. Lyngby, Denmark

ARTICLE INFO

Keywords:
Iron oxide
Nanoparticles
E172
Food pigment

ABSTRACT

Iron oxides used as food colorants are listed in the European Union with the number E172. However, there are no specifications concerning the fraction of nanoparticles in these pigments.

Here, seven E172 products were thoroughly characterized. Samples of all colors were analyzed with a broad spectrum of methods to assess their physico-chemical properties. Small-Angle X-ray Scattering (SAXS), Dynamic Light Scattering (DLS), Transmission Electron Microscopy (TEM), zeta-potential, Inductively Coupled Plasma-Mass Spectrometry (ICP-MS), X-ray diffraction (XRD), Brunauer-Emmett-Teller analysis (BET), Asymmetric Flow Field-Flow Fractionation (AF4) and *in vitro* cell viability measurements were used.

Nanoparticles were detected in all E172 samples by TEM or SAXS measurements. Quantitative results from both methods were comparable. Five pigments were evaluated by TEM, of which four had a size median below 100 nm, while SAXS showed a size median below 100 nm for six evaluated pigments. Therefore, consumers may be exposed to iron oxide nanoparticles through the consumption of food pigments.

1. Introduction

Iron oxides are widely used as industrial food pigments to color sweets, olives or cheese rind (EFSA, 2015). The European Union classifies iron oxides as food additives with the number E172 (EU, 2008). Thereby, no differentiation is made between the different colors: magnetite (Fe_3O_4) is black, FeOOH is yellow, while hematite (Fe_2O_3) can be red or orange-brown, depending on the crystalline structure (Cornell, 2003). However, more detailed labeling is recommended by the panel of the European Union, specifying the molecular structure of the pigment by adding a, b or c as an appendix to E172. Thereby, it can be specified which iron oxide is used (EFSA, 2015).

Iron oxides are generally considered safe food pigments with low acute toxicity. The JECFA (an international scientific expert committee administered jointly by the Food and Agriculture Organization of the United Nations (FAO) and the World Health Organisation (WHO)) set the acceptable daily intake of iron oxides to 0.5 mg/kg bw/day (JECFA, 1980).

In recent years, the concern about the use of nanoparticles in food has risen. Nanoparticles can be intentionally added to food to increase flavor, nutritional value, or shelf life or can be an unintended byproduct of package leaking, attrition or production processes (Bouwmeester et al., 2009; Vance et al., 2015). For pasty food matrices, human exposure is expected to be equal to the total number of particles that are present in the product (Laux et al., 2018). Due to their high surface to volume ratio, they may exhibit altered reactivity compared to comparable bulk materials. Although no new qualitative toxicological properties have been described so far for nanomaterials, their small size facilitates the penetration of the intestinal barrier either by hijacking specific transport systems or by passing through the intercellular space (Oberdörster, Oberdörster, & Oberdörster, 2007). In *in vivo* studies, iron oxide nanoparticles (IONPs) accumulated in liver, spleen and kidney after oral administration, injection, and inhalation (Yang et al., 2015; Zhu et al., 2009).

* Corresponding author.
E-mail addresses: linn.voss@bfr.bund.de (L. Voss), ilunhsiao@tmu.edu.tw (I.-L. Hsiao), maximilian.ebisch@bam.de (M. Ebisch), janvid@food.dtu.dk (J. Vidmar), nadine.dreiack@bfr.bund.de (N. Dreiack), linda.boehmert@bfr.bund.de (L. Böhmert), valerie.stock@bfr.bund.de (V. Stock), albert.braeuning@bfr.bund.de (A. Braeuning), kals@food.dtu.dk (K. Loeschner), peter.laux@bfr.bund.de (P. Laux), andreas.thuenemann@bam.de (A.F. Thünemann), alfonso.lampen@bfr.bund.de (A. Lampen), holger.sieg@bfr.bund.de (H. Sieg).

https://doi.org/10.1016/j.foodchem.2020.127000
Received 10 January 2020; Received in revised form 31 March 2020; Accepted 6 May 2020
Available online 15 May 2020

In the case of E172, information about the physico-chemical characteristics of the pigments is limited. For example, little is known about the particle size distribution in E172 and therefore about the presence of a fraction of nano-sized particles in these food colorants. In addition, knowledge on contamination with other metals is sparse. Therefore, the European Food Safety Authority (EFSA) published a call for scientific data in 2016 to gain detailed knowledge about E172 composition, particle size distribution and toxicological effects. EFSA also published a guidance document on the risk assessment of nanomaterials, which covers detailed advice on how to investigate the size distribution of polydisperse materials (EFSA Scientific Committee, 2018). Such information is needed to assess the human and environmental exposure to nanomaterials and their effects. As a food additive, E172 enters sewage through disposal of food and excretion, and thereby will be found in landfills and surface waters as well (Chen, Wang, Ge, & Guo, 2015). Hence, it is of outmost importance to thoroughly characterize the food grade pigments to determine their fate and effect on the environment.

In this study, we investigated seven different commercially available E172 pigments that were purchased from companies in three different European countries and India. We included two black, two red, two yellow and one orange pigment to compare pigments of different iron oxide structures. Since a broad spectrum of characterization methods is needed to assess physico-chemical properties of food grade pigments, we performed Small-Angle X-ray Scattering (SAXS), Dynamic Light Scattering (DLS), Transmission Electron Microscopy (TEM), zeta-potential measurements, Inductively Coupled Plasma-Mass Spectrometry (ICP-MS), X-ray diffraction (XRD), Brunauer-Emmett-Teller analysis (BET), and Asymmetric Flow Field-Flow Fractionation (AF4). Thereby, the primary particle size and the hydrodynamic diameter were assessed as recommended by the EFSA (EFSA Scientific Committee, 2018). In addition, *in vitro* cell viability measurements were conducted. This data provides information about chemical composition, size distribution, shape, surface charge and the influence of E172 on viability of human gut cells *in vitro*. It was predicted that nanoparticles would be found in the investigated pigments.

2. Materials and methods

2.1. Materials

In total, seven different E172 pigments were obtained. One black, one red and one yellow pigment (labeled Black1, Red1, and Yellow1) were purchased from a company in the United Kingdom, another black (Black2) and red (Red2) pigment were purchased in Germany, the orange pigment (Orange) was purchased from a company in Austria and the second yellow pigment (Yellow2) was obtained from India. All the pigments are used to color foods in industrial processes or in private households. The brands of the food pigments are known to the authors and are available upon request.

If not stated otherwise, other chemicals were purchased from Merck (Darmstadt, Germany), Carl Roth (Karlsruhe, Germany), or AppliChem (Darmstadt, Germany) in the highest available purity.

2.2. Chemical composition

Iron and trace element content was measured by ICP-MS. Therefore, different amounts (up to 1.5 mg) of each pigment underwent acidic digestion using 2 ml 69% HNO_3 in a MLS-ETHOS microwave system (Leutkirch, Germany). Samples were heated at 180 °C for 20 min. After that, samples were filled up to 15 ml with MilliQ water. Using an ICP-MS in scan mode, iron, cadmium, chromium, copper, arsenic, lead, mercury, nickel, and zinc contents as examples for metal contamination were determined. Based on the measured iron content of each sample, the iron oxide content of the dry mass was calculated. Water content was evaluated by drying and weighing. For this purpose, 10 g of pigment were put in an oven for 72 h at 110 °C. The weight loss was attributed to the water content in the sample.

2.3. Particle dispersion

If not stated otherwise, all samples were dispersed in accordance with the NanoGenoTox protocol, which was slightly modified (Jensen et al., 2011): Briefly, the iron oxide samples were prewetted with ethanol (absolute) and then dispersed in a solution of BSA (0.05% (w/w) in MilliQ water). The BSA solution was filtered prior to use (0.22 µm PVDF-GV filter). The dispersion was ultrasonicated for 5:09 min using a Sonopuls HD2200 (equipped with an SH 213 G boosterhorn and a KE 76 extension, Bandelin, Berlin, Germany) resulting in a stock solution with an iron oxide concentration of 2.56 mg/ml.

2.4. Transmission Electron microscopy (TEM), BET and X-ray diffraction (XRD)

For the yellow, orange and red pigments, the samples were taken up in a mixture of 0.3 mM citric acid and 0.5 mM sodium citrate in water in a concentration of 200 µg/ml (S. C. Yang et al., 2014). To reduce agglomeration, the mixtures were treated by using an ultrasonic probe (Microson ultrasonic disruptor, Misonix, USA) at 10 W for 20 min under ice bath. A drop of the final solution (4 µl) was placed on a 200-mesh Formvar coated copper grid and then the sample was dried at room temperature for 18 h. Black pigments were only suspended in absolute ethanol and then dropped onto the copper grid. Representative TEM images were acquired at acceleration voltage 75 kV (Hitachi HT7700, Tokyo, Japan). Briefly, particles were measured manually in length, width and (if spherically shaped) diameter, because they were too polydisperse for automated measuring. Particle size of pigments were measured using ImageJ and R. For the spherical or cube-like particles, the polygon selection was used to define the edge and the particles was measured as Feret diameter. For the rod-like particles, two widest sections of short sides were selected randomly and measured. An average value was used as width. For the long side, a straight line was drawn at the longest visible dimension of the particle and measured. 80 particles were analyzed for each pigment. To show the measurement uncertainty, an interlaboratory comparison between the two laboratories (e.g. BfR and TMU) was done and was expressed as coefficient of variation (CV) to show varieties. Precisely, Lab A and Lab B measured 80 particles from the same images. The particles measured were chosen by the Labs randomly. The resulting data batches were analyzed with R for size distribution density, and minimum, maximum, first and third quartile, as well as median and mean of the dimension of interest (for spherical particles the diameter, for needle-shaped particles the width). For the CV, mean and median for each particle was used.

For BET measurements, the absorption isotherms of the E172 at 77 K (in liquid nitrogen) were measured by using the ASAP 2020 physisorption (Micromeritics Instrument Corporation, GA, USA). Before measurements, the sample was degassed at 120 °C for 150 min in nitrogen gas to remove water or adsorbed gases from the samples, as determined by thermogravimetric analysis (TGA, Mettler-Toledo, 2-HT, Greifensee, Switzerland). Five values of relative pressure range (approximately 0.06 to 0.2) were used to calculate the BET-specific surface area.

The crystalline structures and phases of the E172 pigments were analyzed using an X-ray diffractometer (TTRAX III, Rigaku, Japan). Data was collected in the 2θ range from 10 to 70 °C using Cu Kα radiation. Phases were identified by the Match! Software Version 2 (Crystal Impact, Bonn, Germany).

2.5. Zeta potential and dynamic light scattering (DLS)

To assess the zeta potential and the hydrodynamic diameter, samples were dispersed as described above. For the determination of hydrodynamic diameter, dynamic light scattering was performed. The

dispersion was diluted 1:50 in a 0.05% BSA/water solution and transferred to a DLS cuvette. For zeta potential investigation, the dispersion was diluted in 0.05% SDS and transferred to a capillary cuvette. Both measurements were done with a Zetasizer from Malvern Instruments (Malvern, Worcestershire, United Kingdom).

2.6. Small-angle X-ray scattering (SAXS)

Samples were dispersed as described above. Volumes of 5 × 1 ml of freshly prepared stock solutions were centrifuged at an acceleration of $3773 \times g$ for one minute using an Eppendorf MiniSpin. Afterwards, 5 times 0.8 ml of the supernatant was taken from the vials with an Eppendorf pipette and combined to a total volume of 4 ml.

Small-angle X-ray scattering (SAXS) measurements were performed using a modified Xeuss 2.0 instrument (Xenocs, Sassenage France). X-rays were generated from a microfocus X-ray tube with a copper target, followed by a multilayer optic to parallelize and monochromatize the X-ray beam to a wavelength of 0.154 nm. The instrument had a vacuum motorized detector (Eiger 1 M, Dectris, Baden-Daettwil, Switzerland). The samples with a volume of 4 ml were probed within a flow-through cell under constant flow to avoid sedimentation. The sample cell was equipped with SiN windows. Sample-to-detector distances were 558 mm and 2508 mm. The resulting data were processed using the DAWN software package according to standardized procedures (Filik et al., 2017; Pauw, Smith, Snow, Terrill, & Thunemann, 2017). Data from the different distances were combined into a single curve for ease of interpretation.

For measurement, dispersions were produced from Yellow1, Yellow2, Orange, Red1, Red2 and Black1, while it was not possible to disperse notable amounts of Black2. Within one hour after preparation the dispersions were measured with SAXS as prepared. Data of reasonable quality are found in the q-range between 0.02 nm^{-1} and 1 nm^{-1} from which the upper and lower limit of measurable sizes can be estimated as $d_{max} \approx \pi/0.02 = 160$ nm and $d_{min} \approx 3$ nm. We found that the scattering curves are reproduced well using the analytical form factor of a sphere, $I_s(q, R, \Delta\eta)$, with a log-normal number-weighted size distribution of the radii, $f(R, N, \sigma, \mu)$, as

$$I(q) = \int_0^\infty f(R, N, \sigma, \mu) I_s(q, R, \Delta\eta) dR. \quad (1)$$

Note that the use of more complex data interpretation models was rejected to avoid overfitting. The log-normal size distribution in Eq. (1) is defined as

$$f(N, \sigma, R, R_{median}) = \frac{N}{\sqrt{2\pi}\sigma R} \exp\left(-\frac{\ln(R/R_{median})^2}{2\sigma^2}\right) \quad (2)$$

and the scattering of a single particle is given by

$$I_S(q, R, \Delta\eta) = \left[\frac{4}{3}\pi R^3 \Delta\eta \left(3\frac{\sin(qR) - qR\cos(qR)}{(qR)^3}\right)\right]^2 \quad (3)$$

The R is the sphere radius and $\Delta\eta$ the scattering length density difference between particle and dispersing agent. For the pigments Yellow1 and Yellow2 the $\Delta\eta$ is 2.3366×10^{-11} cm^{-2} when presuming a FeO(OH) stoichiometry, a density of 4.1 g/cm^3 and an X-ray energy of 8.6 keV. Slightly larger is the scattering contrast of Orange with $\Delta\eta = 2.7536 \times 10^{-11}$ cm^{-2} when assuming an equimolar mixture of FeO(OH) and Fe_2O_3. The $\Delta\eta$ is 3.1706×10^{-11} cm^{-2} for Red1 and Red2 with an Fe_2O_3 stoichiometry and a density of 5.25 g/cm^3. The $\Delta\eta$ is 3.1196×10^{-11} cm^{-2} for Black1 with a Fe_3O_4 stoichiometry and a density of 5.20 g/cm^3.

2.7. Light microscopy

To estimate the number of particles that were not dispersed, light microscopy analysis was performed. For this purpose, samples of powders of the particles were spread as thin as possible on microscope slides with a spatula. Images of the dried particles were collected using a Leica DM EP with a 40x/0.65 POL objective and a dhs-MicroCAM 1.3. The images were recorded using the program uEyeCockpit (version 4.22.0000, IDS Imaging Development Systems GmbH). At least 100 particles were assessed from each slide using the open source image processing software ImageJ (version 1.52e, Wayne Rasband National Institutes of Health, USA). Estimation of the number of microparticles from the radii of these particles was performed as follows: The total mass of a pigment, m_1, is known from the initial weight. The mass of non-nano particles, m_3, is m_1 minus the mass of nanoparticles, m_2. The m_2 was determined using SAXSfit from the SAXS data, as described in the interlaboratory comparison (Pauw, Kastner, & Thünemann, 2017). The number of non-nano particles is $n_3 = m_3/m_{3,single}$, where $m_{3,single}$ is the mass of a single non-nano particle. The $m_{3,single}$ can be reasonably estimated since the radii, r_3, of the near-spherical non-nano particles are quite uniform (see light microscopic figures in SI, Fig. S5 (c)). This means that $n_3 = m_3/(4/3\,\pi\, {r_3}^3\, \rho_3)$, where the bulk density, ρ_3, is used as an estimate for the density of the non-nano particles.

All images were converted to 8 bit grey scale images after background subtraction. Positions of the particles on the pictures were marked and their diameters were determined, which were found to be relatively narrowly distributed at about 2 µm (not shown). The mass of each particle was estimated as product of its volume and its density. Here, a spherical geometry was used for volume calculation and it was assumed that the density of the particles corresponds to that of the bulk material. The total mass of the microparticles was calculated as the initial weight minus the mass of the dispersed nanoparticles. The number of microparticles was estimated as the ratio of the mass of all microparticles to the mean mass of a single one (results are shown in Fig. S5 (b)).

2.8. Asymmetric flow field-flow fractionation coupled to multi angle light scattering and inductively coupled plasma-mass spectrometry (AF4-MALS-ICP-MS)

Dispersions of iron oxide pigments were characterized with AF4 coupled to Multi Angle Light Scattering (MALS) for sizing and ICP-MS for identifying the presence of iron. Samples were ultrasonicated as described above and immediately diluted in 0.05% Water-SDS, 1:10 or 1:100. Black1 and Black2 dispersions were not sufficiently stable for AF4 measurements.

The AF4 system consisted of an Agilent 1200 series autosampler (G1329A), a high-performance liquid chromatography pump (G1311A) (Agilent Technologies, Santa Clara, CA, USA), an Eclipse 3 AF4 flow control module, and a short channel-type AF4 separation channel (Wyatt Technology Europe GmbH, Dernbach, Germany). Following separation by AF4, various detectors were used to collect information about the eluting fractions. A DAWN HELEOS TM (Wyatt Technology Europe GmbH, Dernbach, Germany) MALS detector with 17 + 1 observation angles operated with a linear polarized laser light at 658 nm was used to record the light scattering signal. The MALS detector was set to a sampling time interval of 0.5 s per data point. Data from the light scattering detectors was processed using the ASTRA V software (version 5.3.2.15, Wyatt Technology Corporation, Santa Barbara, CA, USA). The final detector in the hyphenated system was an ICP-MS instrument (ICP-QQQ-MS 8900, Agilent Technologies, Tokyo, Japan) was used to record signal intensities of iron (Fe) isotope (m/z 56 - > m/z 56). The instrumental settings are presented in Table S1.

2.9. Cell viability

Influence of E172 food pigments on cell viability of differentiated intestinal Caco2 cells was assessed using the MTT assay. E172 dispersions were prepared using 10 mg pigment/ml stock dispersion and ultrasonification as described. Concentrations for the cell viability assays

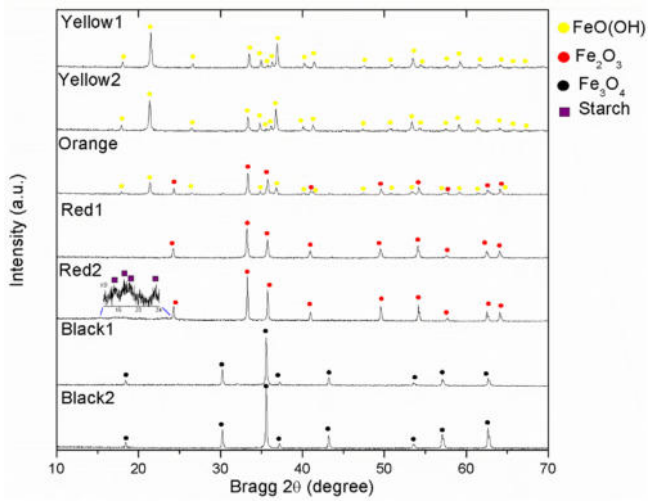

Fig. 1. XRD pattern of E172 samples. All pigments matched well with the expected iron oxide phase. Presence of starch in Red2 was claimed by the supplier and was validated by diffraction patterns between 15 and 23°.

were based on iron content of pigments previously determined by ICP-MS. The MTT assay was performed as described previously (Sieg et al., 2018).

3. Results

3.1. Chemical composition

The iron oxide species present in the different pigments were determined by XRD (Fig. 1). As expected, Yellow1 and 2 matched with FeO(OH), Red1 and 2 with Fe_2O_3 and Black1 and 2 with Fe_3O_4. The orange pigment was a mixture of FeO(OH) and Fe_2O_3 (80.5%:19.5% by fitting, respectively).

The iron content in E172 samples was determined using ICP-MS measurements. Together with the results received by XRD, the total content of the respective iron oxide was calculated. Interestingly, the iron content in samples differed from 12% iron in Red2 to 61% in Black1. The values are shown in Table 1.

ICP-MS allows scanning for other trace elements as well. No significant amount of other trace elements (Cd, Cr, Cu, As, Pb, Hg, Ni, Zn) was detected (Supplementary Material, Table S2). The measured iron oxide content is thus between 17% and 85%, depending on the pigment formulation. The other ingredients of the formulations are manufacturer-specific and no information is available about their composition. It is likely that these components comprise typical filler ingredients and flow enhancers such as starch. In XRD measurements, starch is identified in Red2 via 15, 17, 18 and 23° of diffraction angle 2θ. The patterns and crystallinities are in agreement with previous reports (Kittipongpatana & Kittipongpatana, 2016; Manek, Builders, Kolling, Emeje, & Kunle, 2012; Wang, Wang, Shephard, Wang, & Patindol, 2002).

3.2. BET and zeta potential

BET specific surface area (SSA) was measured using N_2 adsorption. SSA varied from 2.5 (Red2) to 17.3 m^2g^{-1} (Yellow2 and Orange). Multiplying these values with the density of the pigments results in volume-specific surface areas, which are recommended for nanomaterial classification of powders (Wohlleben et al., 2017). The resulting volume-weighted specific surface areas (VSSA) ranged between 13.1 (Red2) m^2cm^{-3} and 80.9 m^2cm^{-3} (Orange). Particle size distribution was not possible to determine by BET, since particles were not spherical and no porosities were determined. Zeta Potential in 0.05% SDS was negative for all pigments with values lower than −30 mV, indicating a modest to good stability in dispersion. Only Red2 depicted a less negative Zeta-Potential. Results are depicted in Table 1. Hydrodynamic diameters in water were assessed by DLS. Since all samples were polydisperse, the polydispersity index as well as the hydrodynamic diameters were quite high, ranging from 0.4 and 401 nm (red 2) to 1 and 4607 (Black1). Values are depicted in Table 1.

3.3. Primary particle size distribution analysis by TEM

Transmission Electron Microscopy (TEM) images were analyzed regarding size distribution using ImageJ. E172 samples are polydisperse mixtures of particles with different shapes, even within same molecular structures. The size distributions found by Lab A can be seen in Fig. 2 (size distributions for Lab B are shown in the Supplementary Material Fig. S1). When more than one shape was observable, all visible dimensions were measured (needle width for FeO(OH) and spherical diameter for Fe_2O_3). For all needles, the aspect ratio was determined, which was 3.1 for Yellow1, 5.7 for Yellow2 and 5.4 for the Orange pigment.

For the yellow and orange pigments, needle-like structures were the most dominant form, black pigments were crystalline and cube- or needle-shaped. The two red pigments differed in their form: while Red1 particles depicted sharp edges and cube-like structures, Red2 particles were round and smooth. For black samples, evaluation of primary particle size distribution was not feasible, since single particle edges were hard to determine due to strong aggregation. However, nanoscaled structures are easy to spot in the different sample images. In all other pigments, nanoparticles were detectable and present in different amounts. Mean and median determined by the interlaboratory

Table 1
Characterization of E172 samples. Seven different iron oxides were analyzed regarding their stoichiometry, iron content and water content. The iron oxide content (mass percent) was calculated afterwards using the determined iron content and the stoichiometry determined by XRD. Iron content was analyzed using ICP-MS, water content was assessed by drying. Specific surface area (SSA) and Volume-Specific Surface Area (VSSA) were assessed using nitrogen adsorption (BET), and zeta potential was determined in 0.05% SDS or water (pH ~ 7) by Laser Doppler Electrophoresis. Z-Average and PdI were determined in water with DLS.

Label	Yellow1	Yellow2	Orange	Red1	Red2	Black1	Black2
Formula	FeO(OH)	FeO(OH)	FeO(OH) + Fe_2O_3	Fe_2O_3	Fe_2O_3	Fe_3O_4	Fe_3O_4
Fe [%] of Formula	63	63	63 + 70	70	70	72	72
Fe [%]	33	43	37	52	12	61	53
FeOx [%]	64	69	57	74	17	85	74
Water [%]	2	2	1.5	0.5	9	0.5	1
SSA [m^2/g]	13.6	17.3	17.3	12.3	2.5	14.2	5.1
VSSA [m^2/cm^3]	55.7	70.9	80.9	64.9	13.1	73.8	26.5
ζ-potential [mV] SDS	−34 ± 1	−37 ± 1	−40 ± 1	−39 ± 1	−16 ± 2	−32 ± 1	−42 ± 1
ζ-potential [mV] H_2O	−25 ± 1	21 ± 1	10 ± 1	−2 ± 1	−20 ± 1	0 ± 1	14 ± 1
Z-Average [nm] H_2O	2003	2063	1763	985	401	4607	3494
PdI H_2O	0.6	0.5	0.9	0.7	0.4	1	1

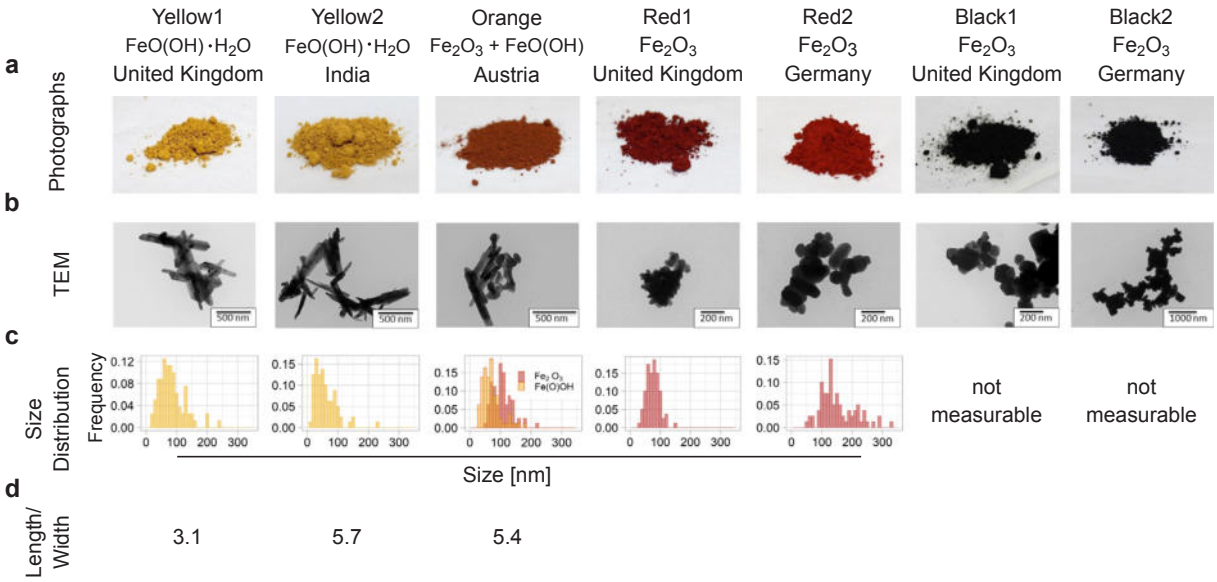

Fig. 2. Size distribution of E172 samples by TEM. Photographs of the E172 pigments (a). TEM images (b), corresponding size distributions measured by Lab A with a binwidth of 10 (c) and the aspect ratio of length to widths of needle-like structures (d). For Yellow1, Yellow2, and Orange, only the width of the needles was assessed. For orange, the spheres were analyzed separately as Fe_2O_3. Black1 and Black2 could not be measured since particle edges are not clear to define in the respective TEM pictures. (For interpretation of the references to color in this figure legend, the reader is referred to the web version of this article.)

Table 2
Overview of the characteristics of E172 samples obtained by TEM and SAXS. TEM images were analyzed regarding particle size distribution using ImageJ. Data results of an interlaboratory comparison. SD = standard deviation, CV = coefficient of variance. In SAXS measurements, diameter and concentration of the particles E172 dispersions were analyzed. The information about the concentration includes number concentration of all dispersed particles, N, number concentration of dispersed nanoparticles N_{nano}, the ratio of nanoparticles with respect to all dispersed particles, N_{nano}/N, the mass concentration of the dispersed particles, c, the concentration of the dispersed nanoparticles, c_{nano}, the weight fraction of nanoparticles with respect to the total mass of the respective colorant, w_{nano}.

		Yellow1	**Yellow2**	**Orange**		**Red1**	**Red2**	**Black1**
		$FeO(OH)$	$FeO(OH)$	$FeO(OH)$	Fe_2O_3	Fe_2O_3	Fe_2O_3	Fe_3O_4
TEM		width [nm]	width [nm]	width [nm]	spheres [nm]	spheres [nm]	spheres [nm]	spheres [nm]
	Median ± SD	78.5 ± 3.5	61.5 ± 17.7	60.0 ± 5.7	103.0 ± 1.4	81.5 ± 7.8	147.0 ± 15.6	-
	CV_{median} [%]	4.5	28.7	9.4	1.4	9.5	10.6	-
	Mean ± SD	87.0 ± 4.2	72.0 ± 18.4	65.5 ± 6.4	105.5 ± 0.7	82.5 ± 9.2	165.0 ± 8.5	-
	CV_{mean} [%]	4.9	25.5	9.7	0.7	11.1	5.1	-
SAXS	Information about the diameter (= 2 x radii) of the particles							
		width [nm]	width [nm]	width [nm]		spheres [nm]	spheres [nm]	spheres [nm]
	Median ± SD	52.1 ± 0.6	82.7 ± 1.2	70.3 ± 1.0		100 ± 2.2	96.5 ± 1.6	54.0 ± 0.8
	Mean ± SD	54.9 ± 0.3	88.9 ± 0.6	73.5 ± 0.5		106.8 ± 1.1	99.6 ± 0.8	57.6 ± 0.4
	Width (%)	35 ± 4	42 ± 5	32 ± 4		40 ± 5	26 ± 3	40 ± 5
	Information on concentration of the particles							
	N (10^9 cm^{-3})	70.8	24.5	37.0		0.68	4.04	16.7
	N_{nano} (10^9 cm^{-3})	69.2	16.7	32.4		0.34	2.2	16.0
	N_{nano}/N (%)	98	68	88		50	55	96
	c (10^{-6} g cm^{-3})	34.1 ± 0.4	57.0 ± 0.8	47.1 ± 0.8		3.4 ± 0.2	13.3 ± 0.2	12.9 ± 0.2
	C_{nano} (10^{-6} g cm^{-3})	29.2	14.5	28.4		0.5	3.5	9.4
	w_{nano} (%)	1.14	0.57	1.11		0.02	0.14	0.37

comparison as well as the corresponding coefficient of variance (CV) can be seen in Table 2. To ensure that the measurements from Laboratory A and B were comparable, boxplots were created in which the measurements per particle and image were compared. An exemplary boxplot can be found in the Supplementary Material for the width of Yellow1 (Fig. S2). Moreover, the 5-factor analysis done by R for each Labs dataset is shown in Table S3 of the Supplementary Material. In three of the five pigments (Yellow1, Yellow2 and Red1) the median was

smaller than 100 nm, indicating a significant amount of nanoparticulate structures. For the orange pigment, the median of the FeO(OH) fraction was below 100 nm, while Fe_2O_3 particles had slightly larger diameters (103 nm).

Dynamic Light Scattering (DLS) was used to determine the hydrodynamic diameter of the samples. However, due to the high polydispersity of the suspensions, the PDI was mainly above 0.6, or showing very high Z-Averages of above 2000 nm, disqualifying the pigments for accurate DLS measurements. It has to be assumed that agglomerates form in ultrapure water and samples are composed of a broad spectrum of particles which is confirmed via TEM measurements.

3.4. Particle size distribution analysis by SAXS

SAXS was employed to determine size, size distribution and concentration of the fractions of the particles which can be transferred from powder to dispersion with the Nanogenotox protocol. Resulting SAXS patterns display a bell-shaped form which is typical for non-interacting particles as can be seen in Fig. S3.

The σ in Eq. (2) is the width parameter of the size distribution and R_{median} is the median radius. Using these parameters, the mean radius was calculated as $R_{mean} = R_{median} e^{\sigma^2/2}$ and the relative standard deviations of the width of the size distributions as $\sigma_{width}/R_{mean} = \sqrt{e^{2\sigma^2} - e^{\sigma^2}}$. Eq. (1) was employed for interpretation of the scattering data of the resulting in fit curves shown in Fig. S3 (solid lines, Supplementary Material). The distribution of the particles' number density in particles per cm^{-3} as probability density function (PDF) and cumulative density function (CDF) are shown in Fig. S4 (solid curves, Supplementary Material). Therein, the mean radii are R_{mean} = 27.4 nm (Yellow 1), 44.5 nm (Yellow 2), 36.8 nm (Orange), 53.4 nm (Red 1), 49.8 nm (Red 2) and 28.8 nm (Black 1). The corresponding relative distribution widths are 35%, 42%, 32%, 40%, 26% and 40%. A summary of these values in terms of diameter (=2 × radius) characteristics is given in Table 2 for easier comparison with the TEM results. The 1st and 3rd quantiles are added to Table S3 of the Supplementary Material.

SAXS allows determination of metrologically traceable sizes but also the measurement of particle number concentrations as proofed recently by national metrological institutes (Schavkan et al., 2019). We used a data evaluation procedure as described in detail earlier (Bressler, Kohlbrecher, & Thünemann, 2015).

For Yellow1 we determined a particle number density of $N = (70.8 \pm 0.9) \times 10^{10}$ cm^{-3} in the suspension. Of these, $N = 69.9 \times 10^{10}$ cm^{-3} (98%) are nanoparticles. The mass concentration of suspended particles is $(34.1 \pm 0.4) \times 10^{-6}$ g cm^{-3}, of which 29.2×10^{-6} g cm^{-3} is from nanoparticles. The mass fraction of nanoparticles which was suspended is 1.14%.

Table 2 presents a list with the respective data for the other colorants.

To assess the number of particles that were not dispersed, light microscopy analysis was performed. Thereby, the number of nanoparticles in the dry powder could be determined (Fig. S5 (b)). Next, the ratio of the nanoparticles to the "non-nano" particles was determined as shown in Fig. 3. It can be seen that the ratios are typically much larger than 1. Additional information about the concentration of nano- and non-nano-particles per gram can be found in the Supplementary Material (Fig. S5).

3.5. Asymmetric flow field-flow fractionation coupled to inductively coupled plasma-mass spectrometry (AF4-ICP-MS)

The main challenge of the AF4-ICP-MS analysis was the preparation of the sample dispersions. Ideally, the dispersions are prepared in the AF4 carrier liquid. For this study, it was decided to use the anionic surfactant SDS at a concentration of 0.05% (m/v) in the carrier liquid. This is a commonly used carrier liquid composition in AF4. The zeta potential of all samples in 0.05% SDS (pH 7.5) was negative (Table 1), which was suitable for AF4-ICP-MS because of the negative surface charge of the membrane. Black1 and Black2 (magnetite) could not be suspended well enough for analysis by AF4-ICP-MS due to the magnetic properties of the particles. Fig. 4 presents the fractograms obtained for the remaining samples. MALS could detect particles with rms diameters in the range of approximately 130 nm to 280 nm. For smaller particles, the scattered light intensity was too low. In all samples, a small mass fraction (< 10%) of particles or aggregates of particles with a hydrodynamic diameter < 100 nm were detected. The amount of the fraction strongly depends on the dispersion efficiency when preparing the samples.

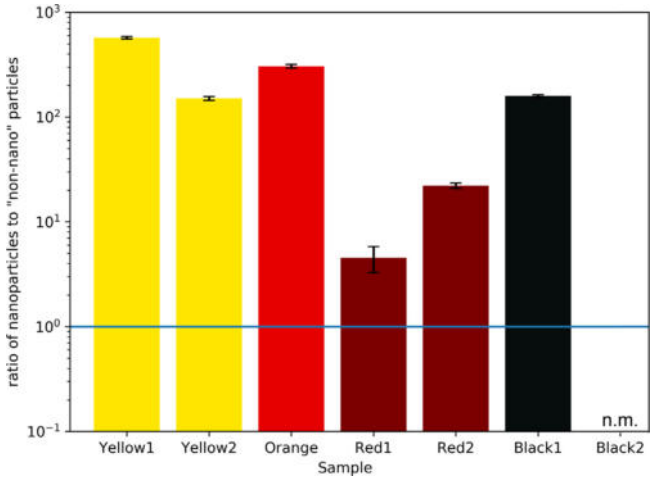

Fig. 3. Ratio of nano to "non-nano"-particles. Number of nanoparticles assessed by SAXS-data was compared to non-nanoparticles determined by SAXS and light microscopy. A ratio equal or above 10^0 indicates a nanomaterial. n.m. = not measurable

Yellow1 dispersed worse than Yellow2 in 0.05% SDS. This resulted in a lower signal and a high peak at the beginning of elution, which was caused by the steric elution of large agglomerates/aggregates. Yellow1 and Yellow2 eluted at later retention times than Red1 and Red2 due to the non-spherical shape of the particles. In the case of gold nanorods with high aspect ratio (> 3), the dynamic elution behavior is defined primarily by the length of the rods (El Hadri, Gigault, Tan, & Hackley, 2018).

The fractogram of Red1 consisted of two peaks. The first peak around 100 nm probably corresponded to primary particles and small aggregates as observed by TEM. The second peak could most likely be attributed to larger agglomerates/aggregates of the particles, which were visible in the dispersions. Red2 eluted, as expected, at a later time than the first peak of Red1 due to the larger particle size (rms diameter of approximately 200 nm at peak maximum). Red2 dispersed well without any observed settling of the particles. Therefore, no additional peak caused by agglomerates was observed.

The fractogram of Orange had a shoulder at a retention time of 10 min besides a main peak with a maximum at around 16 min. This corresponded to the elution of spherical Fe_2O_3 particles (like Red1 or Red2) and FeO(OH) rods (like Yellow1 and Yellow2).

3.6. Cell viability

No cytotoxicity was detected for any E172 sample up to high iron concentrations of 200 µg Fe/ml with the MTT assay. Even when cells were covered with the iron oxide pigments, their viability was not impaired (Fig. S6).

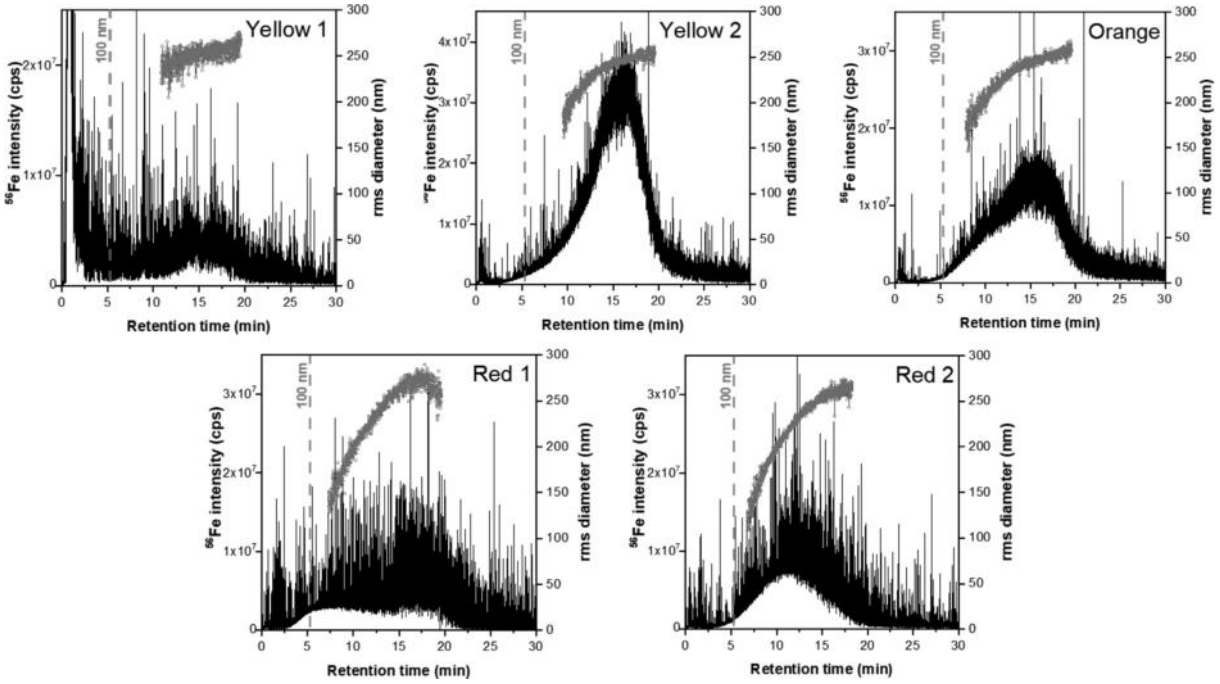

Fig. 4. AF4 fractograms of E172 samples. ICP-MS signal for Fe (black line) and rms diameters determined by MALS (gray circles). The dotted line represents the retention time of polystyrene particles with a hydrodynamic diameter of 100 nm.

4. Discussion

We have investigated seven food-grade iron oxides regarding various physico-chemical properties to characterize the fraction of nanoparticles in the respective pigments. To assess the different characteristics of the pigments, we used a multimethod approach, including TEM, ICP-MS, DLS, XRD, BET, SAXS and AF4. Each of the methods has its own advantages and disadvantages. TEM is a very direct method; however, it gives a picture of several hundred particles only. Moreover, particles can overlap, and edges are hard to distinguish. DLS, SAXS and AF4 are more indirect methods, but give more statistical information. While SAXS can be used for powders and dispersions, DLS and AF4 require the sample to be in dispersion. With BET, especially non-agglomerated and dense particles can be investigated for their size. These methods complement rather than exclude each other and by using them, we could assess the primary particle size as well as the hydrodynamic diameter, as suggested by the EFSA (EFSA Scientific Committee, 2018). For the yellow, orange and red dyes, additional SEM images were taken, but since they do not give further information, they can be found in the Supplementary Material (Fig. S7). Black dyes are magnetic and can therefore not be measured in the SEM instrument.

The iron content of each pigment was investigated using ICP-MS and chemical composition by XRD. While the pigment Red2 was shown to contain less than 20% iron oxide in the form of Fe_2O_3, the main component of Black1 was Fe_3O_4 with an amount of 85%. The main component of Red2 is believed to be starch, as described above. This and other filler ingredients may also explain the high water content of 9%. The zeta potential in ultrapure water varied largely between the samples (Table 1). Even for the same pigment different values were obtained, e.g. −25 mV for Yellow1 to + 21 mV for Yellow2. This indicates different surface modifications of the particles. The isoelectric points of commercially available iron oxides in dilute aqueous solutions of electrolytes are in the range of 3.8 to 9.3 (Kosmulski, 2011, 2014).

Only very small amounts of metals like zinc or trace elements like arsenic could be found, indicating the absence of major pigment contamination. Other components may comprise starch, other filler ingredients or flow enhancers.

Despite of all the different methods used for determination of the nanoparticle fraction, it was especially difficult to measure the black pigments. This is in particular due to their magnetic properties and extensive agglomeration behavior. While Black1 could be measured with SAXS, it was not possible to examine Black2 with any of our methods. Nevertheless, TEM images of both pigments indicate the presence of nanoparticles even though these could not be further characterized. Additional improvements of the dispersion method will be required for these materials.

To answer the question, how many nanoparticles can be found in commercially available E172 pigments, TEM images and SAXS scattering curves provided the most suitable results. Even though agglomeration could be seen in TEM images as well, particles within the agglomerates were detectable and minimum dimensions measurable, showing that nanoparticles were present in the pigments investigated. To express the uncertainty of the data, particle sizes were measured independently by two labs in this study (BfR and TMU, labeled Lab A and Lab B). Coefficient of variance (CV) was under 12%, except for Yellow2. There, the difference in size distribution is bigger, with a CV of 25 and 29% for median and mean, respectively. However, both labs found the widths of the particles to be below 100 nm, so the hypothesis that the material contains nanoobjects in significant amounts is not altered.

When compared to the data acquired by SAXS measurements, the median size of the particles determined by TEM is similar to the median determined by SAXS. Even though differences still exist, both methods show medians with or close to nano-range. Moreover, SAXS data provided insights into the concentration of the nanoparticles, showing that high fractions of dispersable pigment particles are in the nanoscale-range by number, from 50% in Red1 to 98% in Yellow1. It is not surprising that this finding is not represented in mass-percent of nanoparticles (from 0.02% in Red1 to 1.14% in Yellow1), since a few big particles add more weight than a lot of very small ones.

However, in four of five and all measurable samples for TEM and SAXS, respectively, the amounts of nanoparticles detected exceed the definition limit for nanomaterials of the European Union of 50% in at least one dimension (EC, 2011). These results suggest that most iron oxide food pigments could be declared as nanomaterials. However, analytical limitations and inconsistent definitions still apply.

BET is used to determine the surface area of a material based on its nitrogen adsorption isotherm. With this, it is possible to calculate the average particle size but only if particles are spherical, non-porous and not agglomerated during the measurements (Powers, Palazuelos, Moudgil, & Roberts, 2007). The calculation is not accurate especially for needle-shaped particles like seen in the yellow pigments, or mixtures as in the orange sample. Therefore, BET measurements as shown with our samples can help to characterize the material but are not suitable to determine the content of nanoparticles. However, the volume-specific surface area (VSSA) is discussed for regulation affairs to decide on nanomaterials: VSSA values above a threshold value of 60 m^2/cm^3 clearly indicate that a powder is a nanomaterial (Wohlleben et al., 2017). Even though this result is not enough to draw a clear line between nano- and non-nanomaterials as stated above, a VSSA value above 60 was determined for Yellow2, Orange, Red1 and Black1, supporting the aforementioned findings.

Behavior of E172 pigments in dispersions can be investigated by DLS and AF4. However, in DLS, the scattering of bigger particles and few agglomerates mask the scattering of smaller particles, so their signal cannot be detected (Mahl, Diendorf, Meyer-Zaika, & Epple, 2011). Therefore, size distribution of polydisperse samples is hard to assess with this method, coherent with our observations for the iron oxide pigments. Polydispersity Index was between 0.4 and 1 in water, with hydrodynamic diameters ranging from 401 to 4607 nm. Especially for the Black samples, it was not possible to find a solvent or dispersion method preventing agglomeration. These findings do not exclude the presence of nanoparticles, because a few larger particles lead to immense scattering, masking smaller particles easily. Therefore, we would not recommend DLS for polydisperse samples.

AF4 is theoretically more suitable to assess polydisperse samples. Here, we coupled AF4 to MALS and in addition to ICP-MS to ensure peak occurrence in AF4 light scattering was due to iron rather than additional ingredients like starch or other organic compounds. In contrast to the SAXS analysis, no separation of dispersable and non-dispersable fraction was performed prior to analysis. However, it could not be excluded that a certain fraction settled before injection into the AF4 which was consequently not available for analysis. In all samples a small mass fraction ($< 10\%$) of particles or aggregates with a hydrodynamic diameter < 100 nm was determined in agreement with the SAXS results. Further the presence of two fractions was demonstrated in the Orange sample (spheres/needles) and Red1 (potentially small aggregates/large agglomerats). Number-based size distributions are difficult to obtain by AF4-ICP-MS (Correia et al., 2018). Therefore, no attempt was made to determine median particle sizes (based on particle number) for comparison with TEM and SAXS data. The situation was even more complex particles for the needle-shaped FeO(OH), as their shape affects the retention in AF4 as already shown for other particles such as carbon nano-tubes (Moon, Kang, Jung, & Kim, 2004).

We could show the suitability of the different methods to assess characteristics of polydisperse materials. In coherence with the EFSA, findings reported in this study are based on a broad spectrum of methods to determine size distribution. However, we emphasize SAXS as a complementary method to study the size of polydisperse samples.

The presence of nanomaterials in commercial food pigments implicates potential exposure and possible hazards to consumers and workers, as already stated by Yang et al. who showed the occurrence of TiO_2 nanoparticles in commercially available food pigments (Y. Yang et al., 2014). Also exposure of the environment may occur, since iron oxides like E172 are orally ingested and mostly excreted via feces (Singh, Rahman, Murty, Mahboob, & Grover, 2013). The fate of iron oxide nanoparticles in wastewater-plants has not been elucidated fully yet. Hence, nanoparticles derived from E172 could enter the environment via sludge or directly by food disposal and leakage from landfills. How iron oxide nanoparticles affect microorganisms is still under investigation.

In our cell viability assays, no response to any E172 was detectable up to high amounts of iron. However, *in vitro* toxicity tests are not able to cover the full spectrum of toxic mechanisms. Especially the effect of iron oxide nanoparticles on the gastrointestinal system and gut cells is still unclear and needs to be elucidated further.

Iron oxide nanoparticles have been intensively studied. Nevertheless, research on uptake characteristics, biodistribution, interaction with macrophages, or toxicity of iron oxide nanoparticles did not yield uniform results. While most studies report an accumulation of iron oxide nanoparticles in liver and kidney, increased iron concentration in the brain of test animals is also reported in some studies (Singh et al., 2013; Wang et al., 2010). Furthermore, the cellular response to iron oxide nanoparticles is not clearly understood yet. Mechanisms that have been associated with iron oxide nanoparticle exposure include DNA double-strand breaks, impaired formation of neuronal cell morphology and the disruption of cytoskeletal organization (Pisanic, Blackwell, Shubayev, Finones, & Jin, 2007; Sadeghi, Tanwir, & Babadi, 2015). However, the underlying mechanisms are still under investigation. Effects that result from the generation of ROS or mitochondrial damage are under discussion (Gaharwar, Meena, & Rajamani, 2017) and seem to be highly dependent on the nanoparticle species, size, shape, coating, and concentration, underlining the importance of in depth-characterization of different iron oxide nanomaterials using a standardized testing procedure. However, the bioavailability of iron oxides (nano and non-nano) is rather low. For Fe_2O_3 and FeO(OH) there are reports about human uptake from 0.01% up to 10% with and without ascorbic acid, respectively (Derman et al., 1977; Derman et al., 1982). For Fe_3O_4 nanoparticles, reliable data about bioavailability is still missing (EFSA, 2015).

5. Conclusion

In this study, we could show the presence of iron oxide nanoparticles in commercially available E172 samples derived from different countries in high amounts. SAXS and TEM data suggests that more than 50% of the detected particles have at least one external dimension in the size range 1 nm − 100 nm. However, the fraction of nanoscaled particles differs between samples and a classification of a certain pigment as a “nanomaterial” remains questionable due to analytical limitations and inconsistent definitions. Further studies are warranted that use validated methods for a larger set of samples and extend to additional parameters like chemical surface composition and solubility. Since consumers may be exposed to iron oxide nanoparticles, more research is needed to elucidate the cellular responses to them.

Author contributions

Together with Holger Sieg, Albert Braeuning, Linda Böhmert, Valerie Stock and Alfonso Lampen, Linn Voss was responsible for the conceptualization of the present study. I-Lun Hsiao did TEM, SEM, XRD and BET measurements. TEM data evaluation and data visualization of the pictures was done by I-Lun Hsiao and Linn Voss. Andreas Thuenemann and Maximilian Ebert acquired and evaluated the SAXS-data. Janja Vidmar and Linn Voss acquired the AF4-data, visualization and evaluation was done by Janja Vidmar and Katrin Loeschner. Nadine Dreiack and Peter Laux provided ICP-MS data. The first draft was created by Linn Voss. All authors have given approval to the final version of the manuscript.

Declaration of Competing Interest

The authors declare that they have no known competing financial interests or personal relationships that could have appeared to influence the work reported in this paper.

Acknowledgments

I-Lun Hsiao thanks the Taipei Medical University, Taiwan (TMU) for financial support (TMU106-AE1-B27) and the TMU Core Facility for the assistance of TEM operation.

DTU would like to thank Agilent Technologies for providing the 8900 ICP-QQQ instrument. Andreas Thünemann and Maximilian Ebisch thank Glen Smales for help in SAXS measurements.

Appendix A. Supplementary data

Supplementary data to this article can be found online at https://doi.org/10.1016/j.foodchem.2020.127000.

References

Bouwmeester, H., Dekkers, S., Noordam, M. Y., Hagens, W. I., Bulder, A. S., de Heer, C., ... Sips, A. J. (2009). Review of health safety aspects of nanotechnologies in food production. *Regulatory Toxicology and Pharmacology, 53*(1), 52–62. https://doi.org/10.1016/j.yrtph.2008.10.008.

Bressler, I., Kohlbrecher, J., & Thünemann, A. F. (2015). SASfit: A tool for small-angle scattering data analysis using a library of analytical expressions. *Journal of Applied Crystallography, 48*, 1587–1598. https://doi.org/10.1107/S1600576715016544.

Chen, Z. G., Wang, X. J., Ge, Q. L., & Guo, G. C. (2015). Iron oxide red wastewater treatment and recycling of iron-containing sludge. *Journal of Cleaner Production, 87*, 558–566. https://doi.org/10.1016/j.jclepro.2014.10.057.

Cornell, R. M. S., U. (2003). The iron oxides: Structure, properties, reactions, occurences and uses, Second Edition: Wiley-VCH Verlag GmbH & Co. KGaA.

Correia, M. U. T., Philippe, A., & Loeschner, K. (2018). Challenges in determining the size distribution of nanoparticles in consumer products by asymmetric flow field-flow fractionation coupled to inductively coupled plasma-mass spectrometry: the example of Al2O3, TiO2, and SiO2 nanoparticles in toothpaste. Separations, 5(4). doi: 10.3390/separations5040056.

Derman, D., Sayers, M., Lynch, S. R., Charlton, R. W., Bothwell, T. H., & Mayet, F. (1977). Iron absorption from a cereal-based meal containing cane sugar fortified with ascorbic acid. *British Journal of Nutrition, 38*(2), 261–269. https://doi.org/10.1079/bjn19770087.

Derman, D. P., Bothwell, T. H., Torrance, J. D., Macphail, A. P., Bezwoda, W. R., Charlton, R. W., & Mayet, F. G. (1982). Iron absorption from ferritin and ferric hydroxide. *Scandinavian Journal of Haematology, 29*(1), 18–24. https://doi.org/10.1111/j.1600-0609.1982.tb00556.x.

EC. (2011). COMMISSION RECOMMENDATION of 18 October 2011 on the definition of nanomateria. In E. Union (Ed.), Official Journal of the European Union (pp. 275/238-275/240).

EFSA. (2015). Scientific Opinion on the re-evaluation of iron oxides and hydroxides (E 172) as food additives. EFSA Journal (Vol. 13, p. 4317): EFSA Panel on Food Additives.

EFSA Scientific Committee. (2018). Guidance on risk assessment of the application of nanoscience and nanotechnologies in the food and feed chain: Part 1, human and animal health. (Vol. 16). EFSA Journal.

El Hadri, H., Gigault, J., Tan, J. J., & Hackley, V. A. (2018). An assessment of retention behavior for gold nanorods in asymmetrical flow field-flow fractionation. *Analytical and Bioanalytical Chemistry, 410*(27), 6977–6984 < Go to ISI > ://WOS:000447361700002.

EU. (2008). Verordnung (EG) Nr. 1333/2008 des Europäischen Parlaments und des Rates vom 16. Dezember.

Filik, J., Ashton, A. W., Chang, P. C. Y., Chater, P. A., Day, S. J., Drakopoulos, M., ... Wilhelm, H. (2017). Processing two-dimensional X-ray diffraction and small-angle scattering data in DAWN 2. *Journal of Applied Crystallography, 50*, 959–966. https://doi.org/10.1107/S1600576717004708.

Gaharwar, U. S., Meena, R., & Rajamani, P. (2017). Iron oxide nanoparticles induced cytotoxicity, oxidative stress and DNA damage in lymphocytes. *Journal of Applied Toxicology, 37*(10), 1232–1244. https://doi.org/10.1002/jat.3485.

JECFA. (1980). Twenty-third report of the Joint FAO/WHO Expert Committee on Food Additives.

Jensen, K., Kembouche, Y., Christiansen, E., Jacobsen, N., Wallin, H., Guiot, C., … Witschger, O. (2011). The generic NANOGENOTOX dispersion protocol—Standard Operation Procedure (SOP). NANOGENOTOX Deliverable Report No. 3.

Kittipongpatana, O. S., & Kittipongpatana, N. (2016). Physico-mechanical and film-forming properties of carboxymethyl corn starch butyrate.

Kosmulski, M. (2011). The pH-dependent surface charging and points of zero charge V. Update. *Journal of Colloid and Interface Science, 353*(1), 1–15. https://doi.org/10.1016/j.jcis.2010.08.023.

Kosmulski, M. (2014). The pH dependent surface charging and points of zero charge. VI. Update. *Journal of Colloid and Interface Science, 426*, 209–212. https://doi.org/10.1016/j.jcis.2014.02.036.

Laux, P., Tentschert, J., Riebeling, C., Braeuning, A., Creutzenberg, O., Epp, A., ... Luch, A. (2018). Nanomaterials: Certain aspects of application, risk assessment and risk communication. *Archives of Toxicology, 92*(1), 121–141. https://doi.org/10.1007/s00204-017-2144-1.

Mahl, D., Diendorf, J., Meyer-Zaika, W., & Epple, M. (2011). Possibilities and limitations of different analytical methods for the size determination of a bimodal dispersion of metallic nanoparticles. *Colloids and Surfaces a-Physicochemical and Engineering Aspects, 377*(1–3), 386–392. https://doi.org/10.1016/j.colsurfa.2011.01.031.

Manek, R. V., Builders, P. F., Kolling, W. M., Emeje, M., & Kunle, O. O. (2012). Physicochemical and Binder Properties of Starch Obtained from Cyperus esculentus. *Aaps Pharmscitech, 13*(2), 379–388. https://doi.org/10.1208/s12249-012-9761-z.

Moon, M. H., Kang, D. J., Jung, J. H., & Kim, J. M. (2004). Separation of carbon nanotubes by frit inlet asymmetrical flow field-flow fractionation. *Journal of Separation Science, 27*(9), 710–717. https://doi.org/10.1002/jssc.200401743.

Oberdörster, G., Oberdörster, E., & Oberdörster, J. (2007). Concepts of nanoparticle dose metric and response metric. *Environmental Health Perspectives, 115*(6), A290.

Pauw, B. R., Kastner, C., & Thünemann, A. F. (2017). Nanoparticle size distribution quantification: Results of a small-angle X-ray scattering inter-laboratory comparison. *Journal of Applied Crystallography, 50*, 1280–1288. https://doi.org/10.1107/S160057671701010x.

Pauw, B. R., Smith, A. J., Snow, T., Terrill, N. J., & Thunemann, A. F. (2017). The modular small-angle X-ray scattering data correction sequence. *Journal of Applied Crystallography, 50*, 1800–1811. https://doi.org/10.1107/S1600576717015096.

Pisanic, T. R., 2nd, Blackwell, J. D., Shubayev, V. I., Finones, R. R., & Jin, S. (2007). Nanotoxicity of iron oxide nanoparticle internalization in growing neurons. *Biomaterials, 28*(16), 2572–2581. https://doi.org/10.1016/j.biomaterials.2007.01.043.

Powers, K. W., Palazuelos, M., Moudgil, B. M., & Roberts, S. M. (2007). Characterization of the size, shape, and state of dispersion of nanoparticles for toxicological studies. *Nanotoxicology, 1*(1), 42–51. https://doi.org/10.1080/17435390701314902.

Sadeghi, L., Tanwir, F., & Babadi, V. Y. (2015). In vitro toxicity of iron oxide nanoparticle: Oxidative damages on Hep G2 cells. *Experimental and Toxicologic Pathology, 67*(2), 197–203. https://doi.org/10.1016/j.etp.2014.11.010.

Schavkan, A., Gollwitzer, C., Garcia-Diez, R., Krumrey, M., Minelli, C., Bartczak, D., … Shard, A. G. (2019). Number concentration of gold nanoparticles in suspension: SAXS and spICPMS as traceable methods compared to laboratory methods. Nanomaterials, 9(4). https://doi.org/ARTN 502.

Sieg, H., Braeuning, C., Kunz, B. M., Daher, H., Kastner, C., Krause, B. C., ... Lampen, A. (2018). Uptake and molecular impact of aluminum-containing nanomaterials on human intestinal caco-2 cells. *Nanotoxicology, 12*(9), 992–1013. https://doi.org/10.1080/17435390.2018.1504999.

Singh, S. P., Rahman, M. F., Murty, U. S., Mahboob, M., & Grover, P. (2013). Comparative study of genotoxicity and tissue distribution of nano and micron sized iron oxide in rats after acute oral treatment. *Toxicology and Applied Pharmacology, 266*(1), 56–66. https://doi.org/10.1016/j.taap.2012.10.016.

Vance, M. E., Kuiken, T., Vejerano, E. P., McGinnis, S. P., Hochella, M. F., Jr., Rejeski, D., & Hull, M. S. (2015). Nanotechnology in the real world: Redeveloping the nanomaterial consumer products inventory. *Beilstein Journal of Nanotechnology, 6*, 1769–1780. https://doi.org/10.3762/bjnano.6.181.

Wang, J., Chen, Y., Chen, B., Ding, J., Xia, G., Gao, C., ... Wang, X. M. (2010). Pharmacokinetic parameters and tissue distribution of magnetic Fe(3)O(4) nanoparticles in mice. *International Journal of Nanomedicine, 5*, 861–866. https://doi.org/10.2147/IJN.S13662.

Wang, Y. J., Wang, L. F., Shephard, D., Wang, F. D., & Patindol, J. (2002). Properties and structures of flours and starches from whole, broken, and yellowed rice kernels in a model study. *Cereal Chemistry, 79*(3), 383–386. https://doi.org/10.1094/Cchem.2002.79.3.383.

Wohlleben, W., Mielke, J., Bianchin, A., Ghanem, A., Freiberger, H., Rauscher, H., ... Hodoroaba, V. D. (2017). Reliable nanomaterial classification of powders using the volume-specific surface area method. *Journal of Nanoparticle Research, 19*(2), 61. https://doi.org/10.1007/s11051-017-3741-x.

Yang, L., Kuang, H., Zhang, W., Aguilar, Z. P., Xiong, Y., Lai, W., ... Wei, H. (2015). Size dependent biodistribution and toxicokinetics of iron oxide magnetic nanoparticles in mice. *Nanoscale, 7*(2), 625–636.

Yang, S. C., Paik, S. Y., Ryu, J., Choi, K. O., Kang, T. S., Lee, J. K., ... Ko, S. (2014). Dynamic light scattering-based method to determine primary particle size of iron oxide nanoparticles in simulated gastrointestinal fluid. *Food Chemistry, 161*, 185–191. https://doi.org/10.1016/j.foodchem.2014.04.022.

Yang, Y., Doudrick, K., Bi, X. Y., Hristovski, K., Herckes, P., Westerhoff, P., & Kaegi, R. (2014). Characterization of food-grade titanium dioxide: The presence of nanosized particles. *Environmental Science & Technology, 48*(11), 6391–6400. https://doi.org/10.1021/es500436x.

Zhu, M. T., Feng, W. Y., Wang, Y., Wang, B., Wang, M., Ouyang, H., ... Chai, Z. F. (2009). Particokinetics and extrapulmonary translocation of intratracheally instilled ferric oxide nanoparticles in rats and the potential health risk assessment. *Toxicological Sciences, 107*(2), 342–351. https://doi.org/10.1093/toxsci/kfn245.

The Presence of Iron Oxide Nanoparticles in the food pigment E172 - Supplementary Material

Table S1: Parameters for AF4. General parameters are depicted in (a), the separation program is shown in (b) and ICP-MS operating parameters for determination of Fe in (c)

a

Parameters	
Carrier Liquid	0.05 % SDS
Membrane Material	Regenerated cellulose
Channel length	145 mm
Membrane cut-off (kDa)	10
Detector flow (ml/ml)	1
Cross flow (ml/min)	0.3
Focus flow (ml/min)	0.5
Injection flow (ml/min)	0.2
Injection volume (µl)	100

b

AF4 separation program				
Step	Duration (min)	Mode	Cross flow start (ml/ml)	Cross flow end (ml/min)
1	2	Elution with cross flow	0.3	0.3
2	1	Focus flow	/	/
3	2	Injection with focus flow	/	/
4	5	Focus flow	/	/
5	30	Elution with cross flow	0.3	0.1
6	5	Elution without cross flow	/	/
7	5	Injection with elution	/	/

c

Plasma parameters	Type/Value	Cell parameters	Type/Value	Data acquisition parameters	Type/Value
Forward power	1550 W	Gas flow	5.0 mL H_2 min^{-1}	Isotope monitored	$^{56->56}Fe$
Plasma gas flow	15.0 L min^{-1}	Octopole bias	-18.0 V	Scan type	MS/MS
Carrier gas flow	1.1 L min^{-1}	Energy discrimination	0 V	Measurement mode	Time resolved analysis
Sample depth	8.0 mm			Integration time/isotope	0.1 s
Sample uptake flow rate	1.0 mL min^{-1}				

Table S2: Trace element amount. Shown are chromium, nickel, copper, zinc, arsenic, cadmium, mercury, and lead in E172 pigments determined by ICP-MS in mass percent (ppm m/m) n.d. = not detectable

Label	Yellow1	Yellow2	Orange	Red1	Red2	Black1	Black2
Cr	2.7	23.2	1.5	2.0	n.d.	27.7	35.1
Ni	26.1	18.0	62.9	35.7	3.1	46.9	58.8
Cu	n.d.	2.8	n.d.	n.d.	n.d.	0.7	1.0
Zn	147.9	108.0	81.8	126.2	42.7	277.2	33.8
As	0.4	0.1	0.1	0.2	0.1	0.1	0.6
Cd	n.d.	n.d.	n.d.	0.1	n.d.	n.d.	0.1
Hg	n.d.	n.d.	n.d.	n.d.	n.d.	n.d.	n.d.
Pb	0.5	0.9	1.0	1.3	0.4	2.2	2.7

Table S3: Additional data for particle size distribution measurements by TEM and SAXS. Five Factor Analysis done by R for the particle size measurements with TEM images from Lab A and Lab B are in the upper part of the table. Shown are 1st quartile, median, mean, and 3rd quartile for all particles and dimensions that were measurable. For SAXS measurements, 1st and 3rd quartile are added, median and mean can be found in Table 2. All values are given as nanometers [nm].

		Yellow1		**Yellow2**		**Orange**			**Red1**	**Red2**	**Black1**
		FeO(OH)		FeO(OH)		FeO(OH)		Fe_2O_3	Fe_2O_3	Fe_2O_3	Fe_3O_4
Lab A		width	length	width	length	width	length	spheres	spheres	spheres	spheres
	1st quartile	55	175	32	206	49	247	78	59	109	-
	Median	76	224	49	288	64	364	102	76	136	-
	Mean	84	284	59	327	70	370	105	76	159	-
	3rd quartile	99	364	79	396	81	480	123	90	193	-
Lab B		width	length	width	length	width	length	spheres	spheres	spheres	spheres
	1st quartile	48	175	53	257	43	197	77	70	115	-
	Median	81	311	74	347	56	335	104	87	158	-
	Mean	90	316	85	375	61	327	106	89	171	-
	3rd quartile	132	458	109	493	73	443	125	104	218	-
SAXS		width		width		width			spheres	spheres	spheres
	1st quartile	42		64		57.4			78.4	81.6	42.3
	3rd quartile	64.7		106.9		86			127.6	114.3	68.9

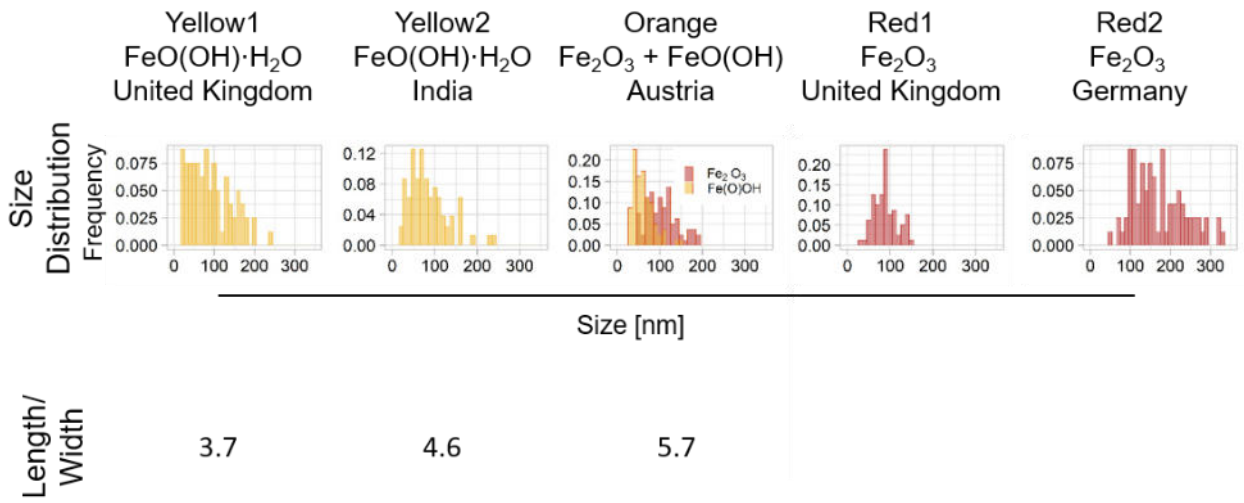

Figure S1: Size distribution of E172 samples by TEM. Shown are the measurements by Lab B with a binwidth of 10, and the aspect ratio of length to widths of needle-like structures. For Yellow1, Yellow2, and Orange, only the width of the needles was assessed. For orange, the spheres were analyzed separately as Fe_2O_3. Black1 and Black2 could not be measured since particle edges are not clear to define in the respective TEM pictures.

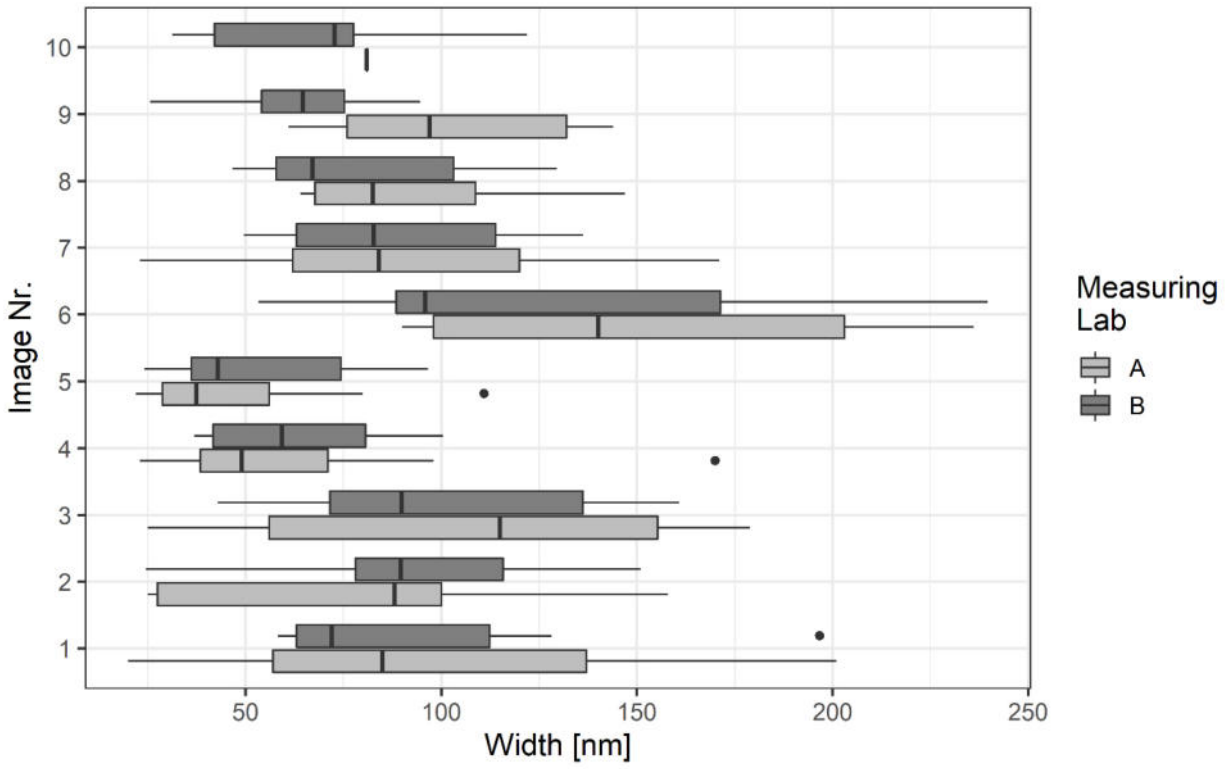

Figure S2: Comparison of particle measurement by Lab A and Lab B. For Yellow1, all width-measurements from all evaluated pictures were compared. Pictures were indexed with a number. Boxplots show that data is consistent in the interlaboratory comparison.

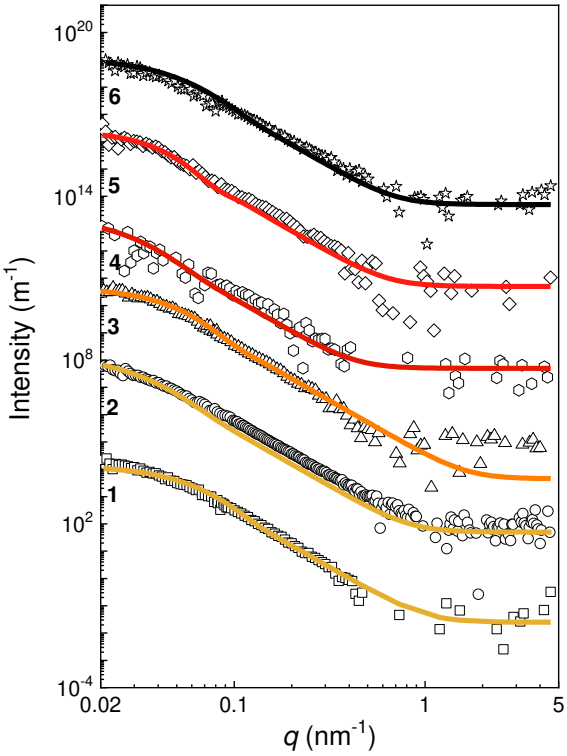

Figure S3: Experimental SAXS data and curve fits. The experimental data are displayed as symbols and the model curves are displayed as solid lines. The scattering intensity, *I*, is plotted as a function of the modulus of the scattering vector, *q*, on a double logarithmic scale. Data and model curves are appropriately displaced along the intensity axis for better visualization. (1) Yellow1, (2) Yellow2, (3) Orange, (4) Red1, (5) Red2, (6) Black1 (line colors indicate the visual color appearance of the samples). Data and curves are shifted vertically for better visibility.

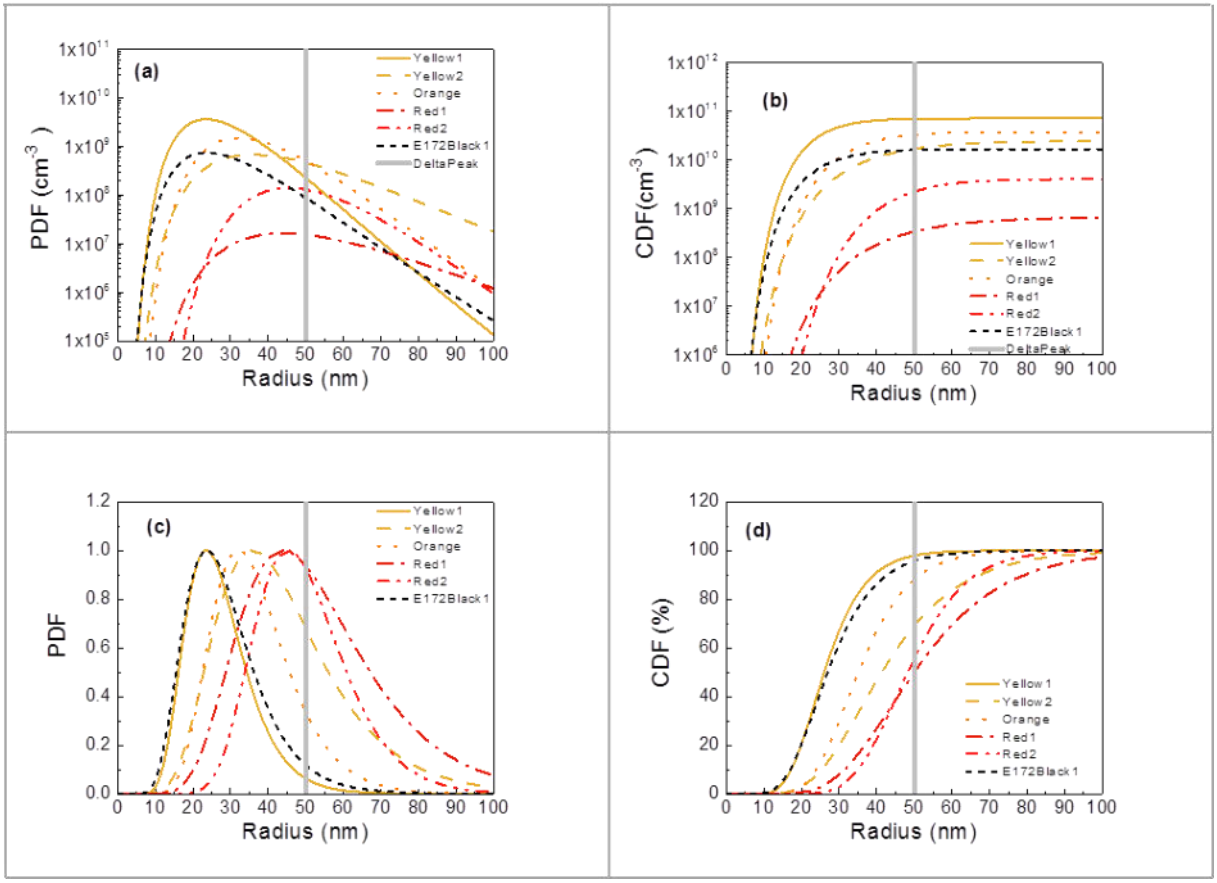

Figure S4: Radii distributions of E172 samples. The partial differential functions are displayed, PDF ((a) and (c)) and cumulative distribution functions, CDF ((b) and (d)). The number-weighted distributions in (a) and (b) are given in units of particles per cm^3 on a logarithmic scale. The PDFs in (c) are normalized to their peak maxima and the CDFs in (d) are provided in % of their maximum values for ease of comparison. The vertical grey line marks the boundary between nanoparticles and not nanoparticles.

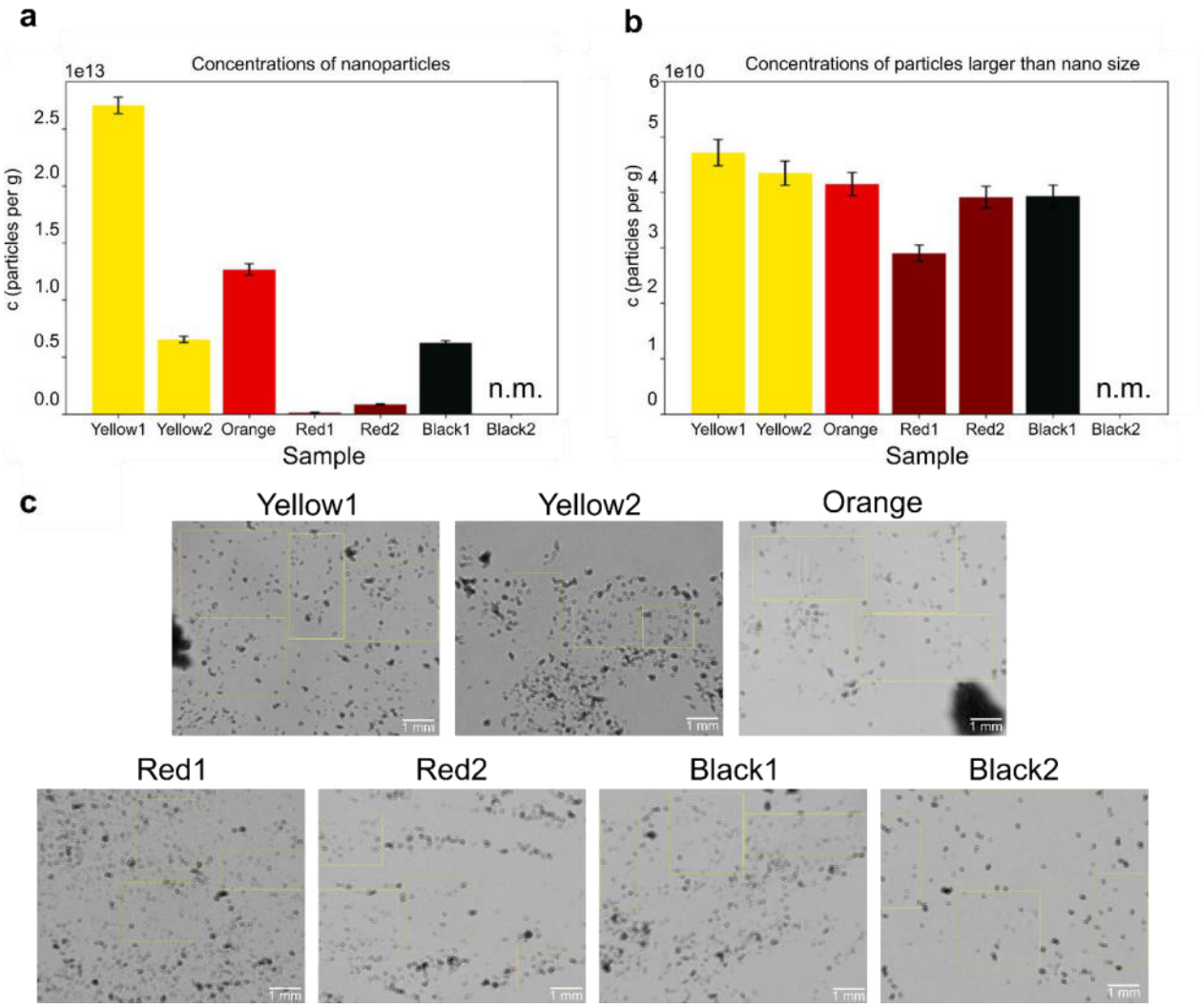

Figure S5: Concentration of nano- and non-nanoparticles in E172 pigments. SAXS-measurements as well as light microscopic pictures were used to calculate the number of particles per gram for (a) nano- and (b) non-nanoparticles in the different pigments. These values were used to obtain the ratio of nano- to non-nanoparticles depicted in Figure 5. n.m. = not measurable. (c) Light Microscopy Pictures of E172 pigments to determine the amount of microparticles. Yellow rectangles indicate evaluated areas. Scale represents 1 mm.

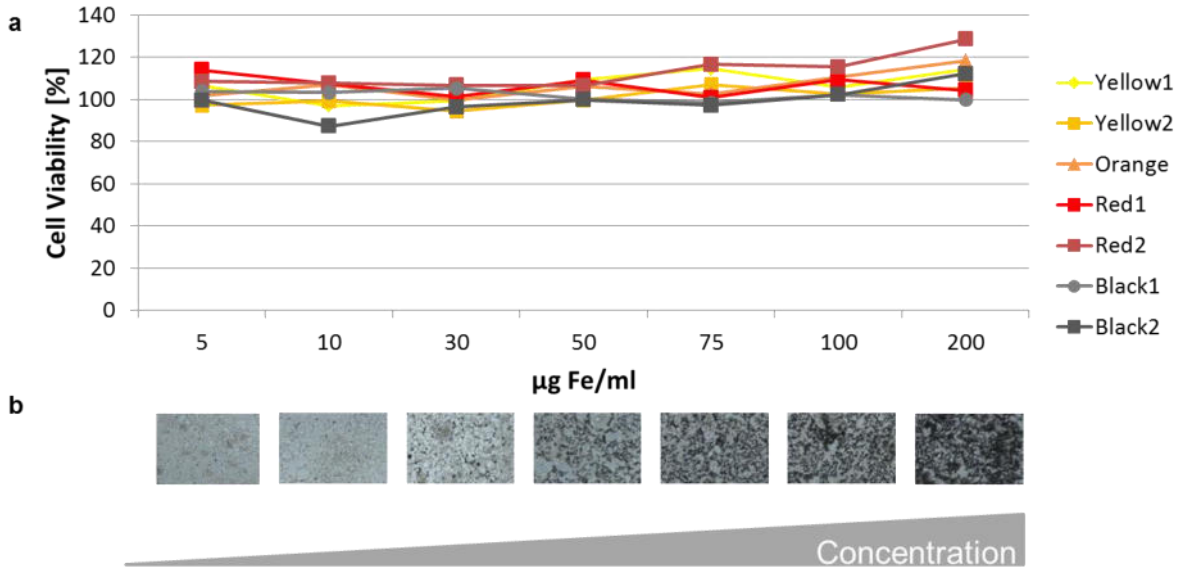

Figure S6: E172 pigments do not impact cell viability of Caco-2 cells. Caco-2 cells were incubated with increasing concentrations of E172. (a) Cell viability was assessed using the MTT assay. (Mean of n=3), Statistical analysis was done by ONE-WAY ANOVA with significance of $p < 0.05$. (b) Microscopic images of cell coverage by particles were taken for all concentrations; here, Black1 is depicted.

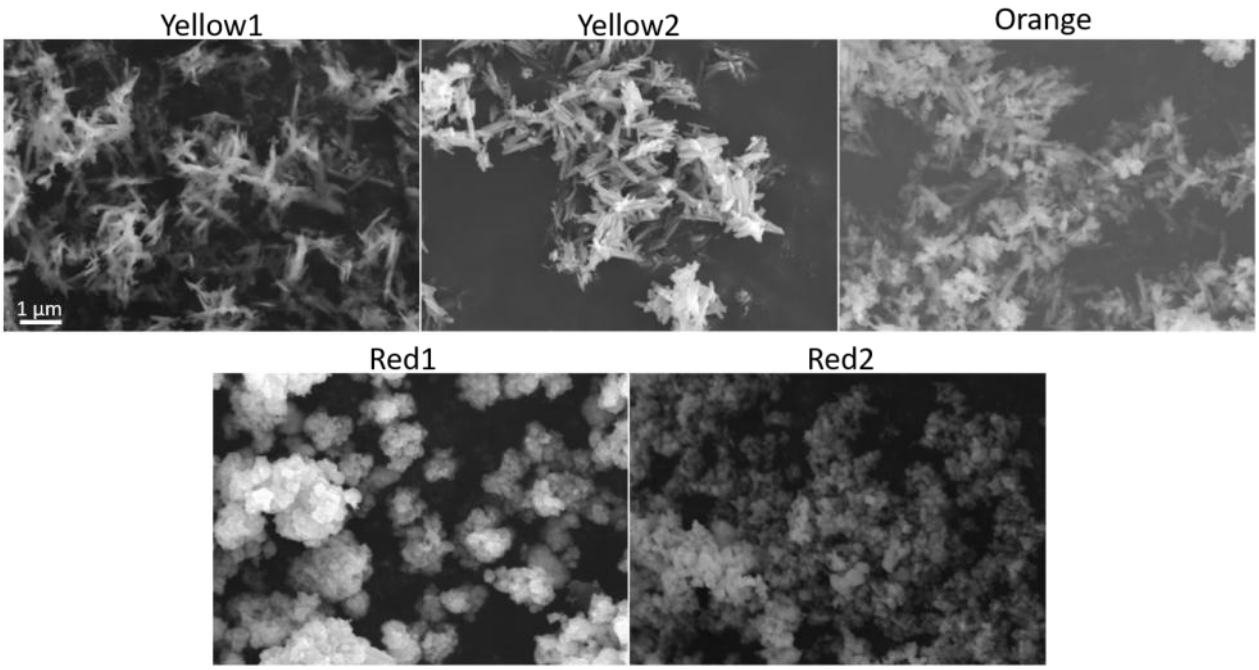

Figure S7: SEM images of Yellow1, Yellow2, Orange, Red1, and Red2. SEM secondary electron (SE) images were acquired at acceleration voltage 15 kV (Hitachi SU3500, Tokyo, Japan). Pigments were sprinkled onto double-sided conductive carbon adhesive tapes without metal coating. Black samples are not measurable in the instrument due to their magnetic properties. Particle size distribution could not be measured with SEM-pictures.